

A failed wind candidate in NGC 3783 from the 2001 year campaign with Chandra/HETGS

Chen Li^{1,2}, Jelle S. Kaastra^{1,2}, Liyi Gu^{2,1}, Daniele Rogantini³, Anna Juráňová⁴,
Missagh Mehdipour⁵, Jelle de Plaa²

¹ Leiden Observatory, Leiden University, PO Box 9513, 2300 RA Leiden, the Netherlands
e-mail: cli@strw.leidenuniv.nl

² SRON Netherlands Institute for Space Research, Niels Bohrweg 4, 2333 CA Leiden, The Netherlands

³ Department of Astronomy and Astrophysics, The University of Chicago, Chicago, IL 60637

⁴ MIT Kavli Institute for Astrophysics and Space Research, Massachusetts Institute of Technology, Cambridge, MA 02139, USA

⁵ Space Telescope Science Institute, 3700 San Martin Drive, Baltimore, MD 21218, USA

ABSTRACT

We reanalyze the Chandra/HETGS observations of NGC 3783 from the campaign in the year 2001, identifying significant spectral variations in the Fe unresolved transition array (UTA) over timescales of weeks to months. These changes correlate with a 1.4 – 2 fold increase in the ionizing continuum and exceed 10σ significance. The variations primarily originate from a low-ionization state ($\log\xi = 1.65$) component of the warm absorber. Time-dependent photoionization modelling confirms the sensitivity of this low-ionization component to continuum variations within the Fe UTA band. Local fitting indicates a lower density limit of $> 10^{12.3} \text{ m}^{-3}$ at 3σ statistical uncertainty, with the component located within 0.27 pc. Our findings suggest that this low-ionization component is a potential failed wind candidate.

Key words. X-rays: galaxies – galaxies: active – galaxies: Seyfert – galaxies: individual: NGC 3783

1. Introduction

NGC 3783, a nearby Seyfert 1 galaxy at redshift $z = 0.009730$ (Theureau et al. 1998), hosts one of the most luminous local AGNs, with bolometric luminosity of $\log L_{\text{AGN}} \sim 44.5 \text{ erg s}^{-1}$ at a distance of 38.5 Mpc (Davies et al. 2015). The AGN is powered by a supermassive black hole with $M_{\text{BH}} = 2.82^{+1.55}_{-0.63} \times 10^7 M_{\odot}$ (Bentz et al. 2021). Extensive studies have focused on its ionized outflow, particularly the X-ray warm absorbers near the nucleus. While near-infrared interferometry has partially resolved the spatial structure of the broad-line region (BLR) within the central parsec (GRAVITY Collaboration et al. 2021), the lack of direct imaging limits precise distance measurements of ionized plasma, including the warm absorber. This limits our ability to accurately determine the kinetic power and mass outflow rate of these absorbers.

The ionization parameter

$$\xi = \frac{L_{\text{ion}}}{n_{\text{H}} r^2}, \quad (1)$$

serves as a proxy for the outflow distance from the ionizing source, where L_{ion} is the ionizing luminosity over the 1-1000 Ryd range, n_{H} is the hydrogen number density, and r is the distance from the ionizing source (Tarter et al. 1969, Krolik et al. 1981). By measuring ξ , L_{ion} , and n_{H} , we can indirectly estimate the distance of the outflow.

Two main approaches can be used to derive the density for AGN outflows. The first relies on density-sensitive metastable spectral lines, which require high-quality, high-resolution spectra (often from time-averaged observations). For example, using the spectral energy distribution (SED) of NGC 5548, Mao et al. (2017) studied density diagnostics for AGN outflows through

metastable absorption lines of Be-, B-, and C-like ions, showing that different ions within the same isoelectronic sequence can cover a broad range of ionization parameters and densities. This technique has been used successfully to constrain the density of the lower ionized gas in NGC 3783 using UV lines (Gabel et al. 2005).

As another approach, the spectral-timing method uses time-resolved spectra to analyze plasma responses to fluctuations in ionizing luminosity (Kaastra et al. 2012, Silva et al. 2016, Juráňová et al. 2022). Time-dependent photoionization modeling provides a comprehensive framework, simultaneously solving for ion concentration, heating, and cooling evolution in response to SED and AGN variability (Rogantini et al. 2022, Sadaula et al. 2023). The evolution of plasma state, indicated by average charge over time, is driven by the relationship between the variability timescale (t_{var}) and the recombination timescale (t_{rec}), where t_{rec} is inversely proportional to plasma density. When t_{var} and t_{rec} are comparable, measurable lag timescales emerge between ionizing luminosity changes and plasma state variations, given adequate sampling and photon counts in individual spectra (Li et al. 2023).

Variability in spectral lines correlated with flux changes has been observed in high signal-to-noise, high-resolution absorption spectroscopic studies (Netzer et al. 2003; Krongold et al. 2005). Analyzing the 900 ks Chandra/HETG spectrum of NGC 3783, Kaspi et al. 2002 provided a comprehensive characterization of the absorption spectrum, which included several significant iron features, such as the L-shell lines from Fe xvii to Fe xxiv, as well as the Unresolved Transition Array (UTA) of M-shell lines. The distinct Fe UTA structure has also been detected in XMM-Newton RGS spectra (Behar et al. 2001; Blustein

et al. 2002). Various photoionization models have been applied to analyze the X-ray absorption spectra of NGC 3783, employing different configurations: two ionized components (Blustin et al. 2002; Krongold et al. 2003; Krongold et al. 2005), three components (Netzer et al. 2003), five components (Ballhausen et al. 2023), and nine components (Mehdipour et al. 2017; Kaastra et al. 2018; Mao et al. 2019). These models typically assumed photoionization equilibrium. However, Gu et al. (2023) introduced time-dependent effects within a nine-component photoionization model, constraining the warm absorber’s density to the range $10^{10} - 10^{13} \text{ m}^{-3}$.

Using the new time-dependent photoionization model, `tpho` (Rogantini et al. 2022), in the SPEX code (Kaastra et al. 2024), we perform a self-consistent calculation of the full time-dependent ionization state for all ionic species, generating synthetic transmission spectra based on the observed light curve.

The structure of the paper is as follows. Section 2 presents the data reduction process for the Chandra/HETGS observations, incorporating recent calibration updates and displaying the resulting ratio spectrum. We also use the long-term RXTE light curve to calibrate the six Chandra observations to RXTE’s flux level. Section 3 describes our application of the `tpho` model to analyze the Chandra grating data of NGC 3783. Section 4 summarizes the findings from our analysis. Finally, Section 5 discusses the results and potential model dependencies.

2. Data Reduction

We used the CIAO v4.15 software and calibration database (CALDB) v4.10 to reprocess the Chandra/HETGS data. The `chandra_repro` script was employed to screen the data and generate spectral files for each observation. We combined the +1st and -1st orders of the medium-energy grating (MEG) spectra using the CIAO tool `combine_grating_spectra`, along with the associated response files, to produce an averaged MEG spectrum for each observation, with Gehrel’s errors applied.

Next, we used the HEASoft `mathpha` tool to convert Gehrel’s errors to Poisson errors and the `spextools` `trafo` utility to transform the OGIP spectral format into the SPEX data input format.

To minimize systematic uncertainties, we utilize only the first-order Chandra/MEG spectrum, as the second and third orders are too faint to significantly contribute to the photon count. Fig. 1 displays the resulting spectra for the five observations from the 2001 campaign, with the Fe UTA feature clearly visible in the high-flux observation (ObsID 2093).

To investigate potential line variability, we calculate ratio spectra by comparing the high-flux state (ObsID 2093) to four lower-flux states (ObsIDs 2090, 2091, 2092, and 2094), which were observed within approximately one to three months of the high-flux state.

To account for the effect of continuum variation, we normalize the low-flux data to the high-flux state based on the average flux in the 9 – 14 Å band. The resulting ratio spectrum between ObsID 2090 and ObsID 2093 is presented in Fig. 2.

To construct a continuous light curve, we combine RXTE/PCA and Chandra/HETGS data, as shown in Fig. 3. Chandra/HETGS fluxes are converted to the equivalent RXTE 2–60 keV flux using WebPIMMS, assuming a power-law continuum and a Galactic absorption column density of $8.7 \times 10^{20} \text{ cm}^{-2}$ (Alloin et al. 1995). The converted flux levels are provided in Table 1. The Chandra observations analyzed in this study are marked in red in Fig. 3, plotted at the midpoint of each exposure. For reference to long-term variability, we also include the

Table 1: Observation log. t_{exp} : exposure time of Chandra observation. t_{gap} : the time gap between two adjacent Chandra observations. The fifth column shows the averaged Chandra flux for each observation. RXTE flux (last column) in the 2 – 60 keV band.

ID	start time (UTC) yyyy-mm-dd	t_{exp} (ks)	t_{gap} (days)	Chandra ave. flux (5-20)Å (cts/s/m ² /Å)	RXTE flux (2-60 keV) (cts/s/PCU)
373	2000-01-20	56		6.26	9.507
2090	2001-02-24	166	369d	4.10	6.505
2091	2001-02-27	169	3d	4.01	6.405
2092	2001-03-10	165	11d	4.81	7.118
2093	2001-03-31	166	21d	8.98	11.58
2094	2001-06-26	166	108d	5.59	8.389

observation taken in 2000 (ObsID 373) to illustrate the long-term timescale.

3. Method

To investigate the spectral variability, we employ the `tpho` model (Rogantini et al. 2022) of SPEX (v3.08.01; Kaastra et al. 1996; Kaastra et al. 2024). Following Li et al. (2023), the initial unobscured SED is derived from the average broadband spectrum presented by Mehdipour et al. (2017) with no assumed changes in SED shape over time. The nine warm absorber components identified by Mao et al. (2019) are implemented within `tpho`, with their equilibrium properties serving as initial conditions. To capture the effects of long-term variability, we trace the evolution of each warm absorber component, extending sufficiently far back in time, guided by the up to weeks of RXTE monitoring preceding the Chandra observations are shown in Fig. 4.

Each component is exposed to the same unobscured SED, with light curves varying according to the observed data. This approach enables us to assess how flux amplitude influences the resulting absorption spectra. The simulated transmissions are then cosmologically redshifted and convolved with the MEG response function. Finally, we derive the model ratio between low- and high-flux states from the simulated transmissions, with each state normalized separately to its respective continuum level.

4. Results

The ratio spectrum in Figure 2 reveals distinct features corresponding to the rest frame wavelengths of the Ne ix resonance line (13.447 Å), the Fe UTA absorption complex (16 – 17 Å), the narrow O vii radiative recombination continuum (RRC at the O vii edge, 16.771 Å), the O vii absorption edge (16.771 Å), and the O vii/O viii absorption lines (18.627 Å and 18.973 Å, respectively). As the Ne emission lines are relatively narrow, they are likely stable over time, appearing to deviate from unity due to the ratio spectrum’s normalization against a variable continuum. And the optical depths of O vii Ly β , O viii Ly α , Ne ix resonance line are very large, which indicate that all of these absorption lines are saturated. In contrast, the Fe UTA absorption complex and the O vii edge (16 – 17.5 Å in the observed frame) exhibit significant variability, serving as the primary diagnostic indicators of warm absorber variation. By fitting the ratio spectrum with a combination of positive and negative Gaussian components, we determine a 10σ significance for Fe UTA variation, consistent with findings by Krongold et al. (2005).

Figure 5 demonstrates that component 5, with $\log \xi = 1.65$ and column density = $0.5 \times 10^{26} \text{ m}^{-2}$, is the main contributor

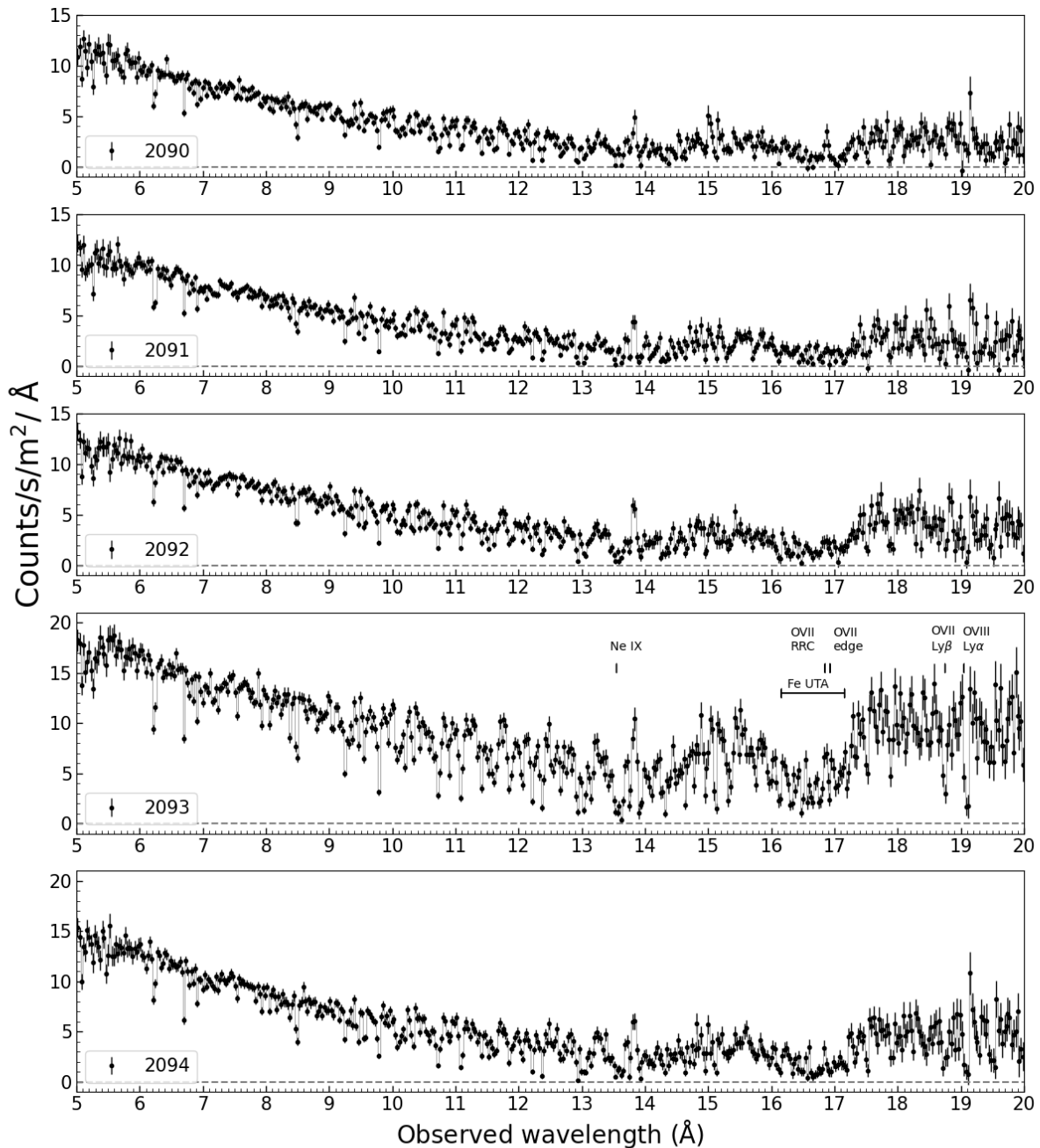


Fig. 1: Chandra/HETGS observations in 2001 binned at 0.03 \AA .

to the Fe UTA complex and O VII edge. The spectral variations observed in the ratio spectrum (Figure 2) reflect an increase in optical depth at the long-wavelength end of the Fe UTA and the O VII edge during the low-flux state, suggesting a response of the ionization state of the warm absorber.

Figure 6 displays the results from the `tpho` calculations for component 5 and the best fit to the observed ratio of ObsID 2090 over 2093 within the local wavelength range of $15 - 18 \text{ \AA}$. Panel (a) shows a clear transmission change from low-flux (red) to high-flux (blue) states at the same density, with the transmission

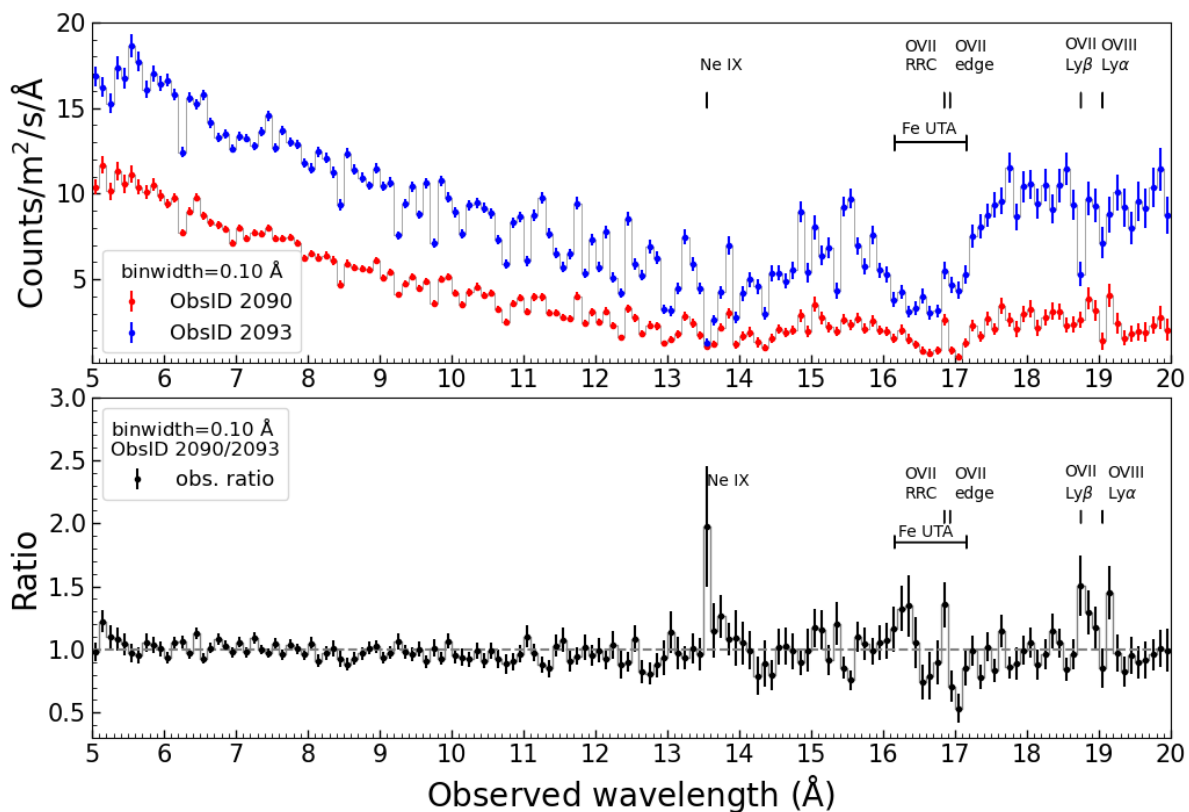


Fig. 2: Top: low flux state ObsID 2090 and high flux state ObsID 2093 spectra binned to 0.1 Å. Bottom: The low flux state ObsID 2090 is scaled up by a factor of 2.21, and the ratio spectrum is defined by the low flux state over the high flux state ObsID 2093.

ratio (black) revealing prominent peaks and dips exceeding 20% within the 16 – 17 Å wavelength range.

Panel (b) of Figure 6 shows that calculations at lower densities (purple) produce weaker or negligible variations within the 16 – 17.5 Å band, which is attributed to longer recombination timescales and reduced variability in ionization structure. In contrast, higher-density calculations (red and yellow lines) amplify the contrast between low- and high-flux states, with the greatest amplification occurring at a density of $10^{13.4} \text{ m}^{-3}$, the current limit of our computational capabilities.

Panel (c) of Figure 6 demonstrates that a density of $10^{13.4} \text{ m}^{-3}$ is optimal for reproducing the observed UTA and O VII edge variations, as suggested by the *tpho* calculations for component 5. Figure 2 displays a peak in the ratio spectrum corresponding to the narrow O VII RRC at 16.85 Å in the observed frame. To interpret this feature, we assume that the RRC component remains constant over time, with the peak arising solely from continuum variation. This assumption is reasonable, as the RRC likely originates from the narrow line region, which is characterized by low density (estimated around 10^{10} m^{-3} , Davies et al. 2020) and thus has a recombination timescale of approximately one year (see Table 4 of Li et al. 2023). In panel (c), the red line representing the model ratio under this assumption agrees well with the observed data. The green line showing the *tpho* calculation without adding O VII RRC ratio gives a poorer fit. Additionally, we present the *pion* model calculation (purple), which closely matches the *tpho* results at a density of

$10^{13.4} [\text{m}^{-3}]$ within the Fe UTA band. However, slight discrepancies are noted around the O VII edge band, with the *pion* model displaying a slightly lower continuum level than *tpho*. This suggests additional continuum absorption in the *pion* calculation, likely arising from oxygen within this wavelength range. We will explore this aspect in greater detail in the subsequent discussion.

In addition to component 5, component 6 might also partially contribute to the Fe UTA and O VII edge structure (see Fig. 5). However, our *tpho* calculations reveal that variations in component 6 are relatively minor, showing changes of less than 10%, especially when compared to the more substantial variability predicted for component 5.

To further constrain the density of component 5, we conducted a joint analysis of the ratio spectra from all four low-flux observations (ObsIDs 2090, 2091, 2092, and 2094) relative to ObsID 2093 within the 15 – 18 Å range. Figure 7 presents the ratio spectra (in black), fitted with the Component 5 model (in green), the Component 5 model including RRC (in red) with a density of $10^{13.4} \text{ m}^{-3}$, and the *pion* model (in purple). Unlike ObsID 2090, the other three ObsIDs do not exhibit strong variation in ratio structure. Specifically, for ObsID 2094, the *tpho* model ratio for component 5 aligns well with the *pion* model, suggesting that the observed variations are within the expected range at this density level.

For component 5 ($\log \xi = 1.65$), we performed a series of *tpho* calculations across a density range from 10^8 to 10^{15} m^{-3} . For each density, we calculated a chi-square value by comparing

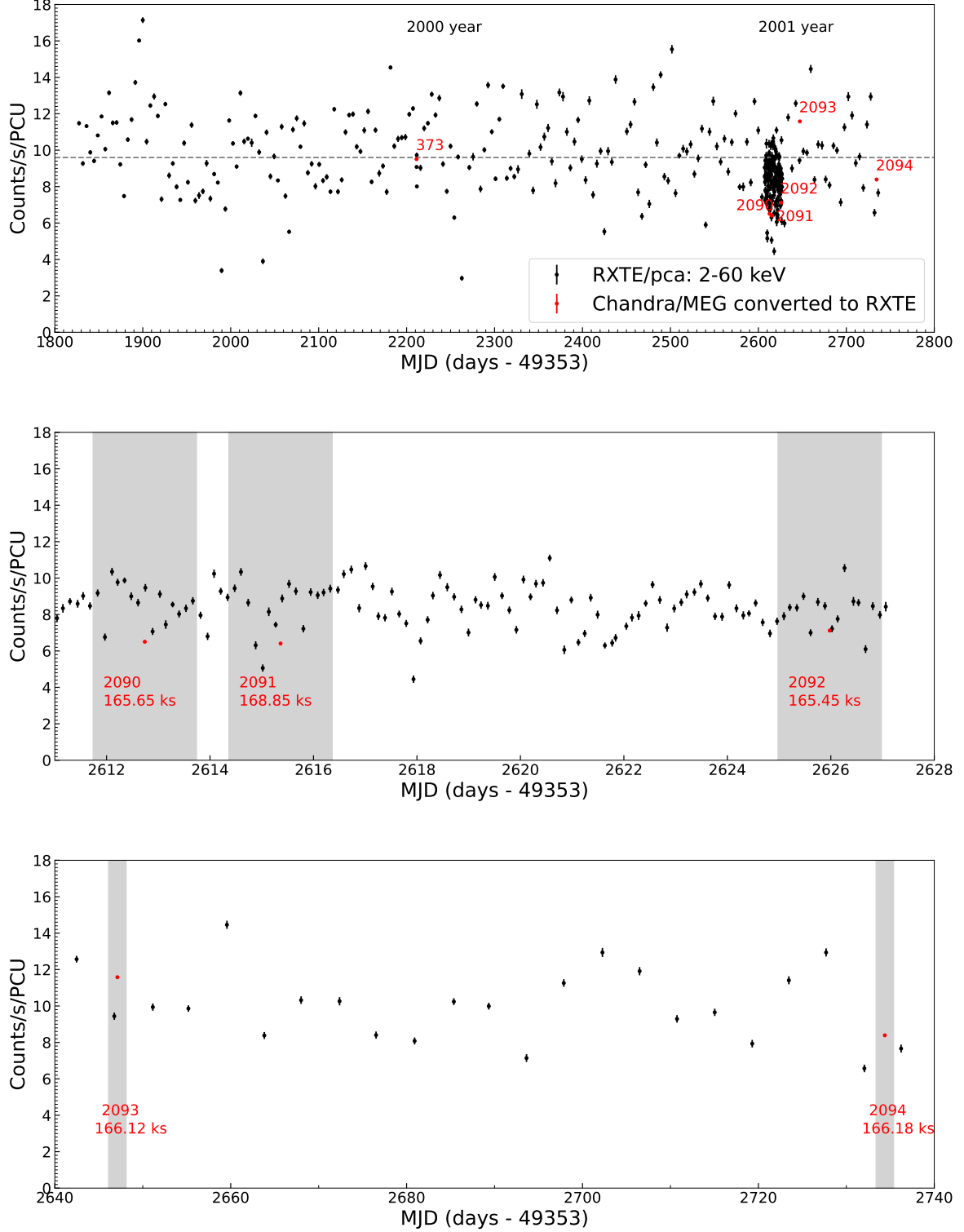


Fig. 3: RXTE light curve of NGC 3783 together with the epochs of 6 Chandra observations. Top panel: the horizontal line represents the average flux level over 1.5 years of RXTE observations. Light gray shade bars represent the epochs of the Chandra observations.

the model predictions to the observed ratio spectra (Figure 8). Because the sampling of the input light curve for ObsID 2094 is sparse (2×10^5 s) especially in last two weeks, it cannot give a reliable constraint for densities $\geq 10^{12} \text{ m}^{-3}$ for oxygen, densities $\geq 10^{10.3} \text{ m}^{-3}$ for iron corresponding to the recombination

timescale of 2×10^5 s for that density, separately (see vertical dashed lines of Figure 9 and refer to Li et al. 2023). For the remaining observations, the sampling time is much shorter, of the order of 10^4 s (see Fig. 4), and we get reliable predictions for densities up to 10 m^{-3} . Again, for higher densities the sam-

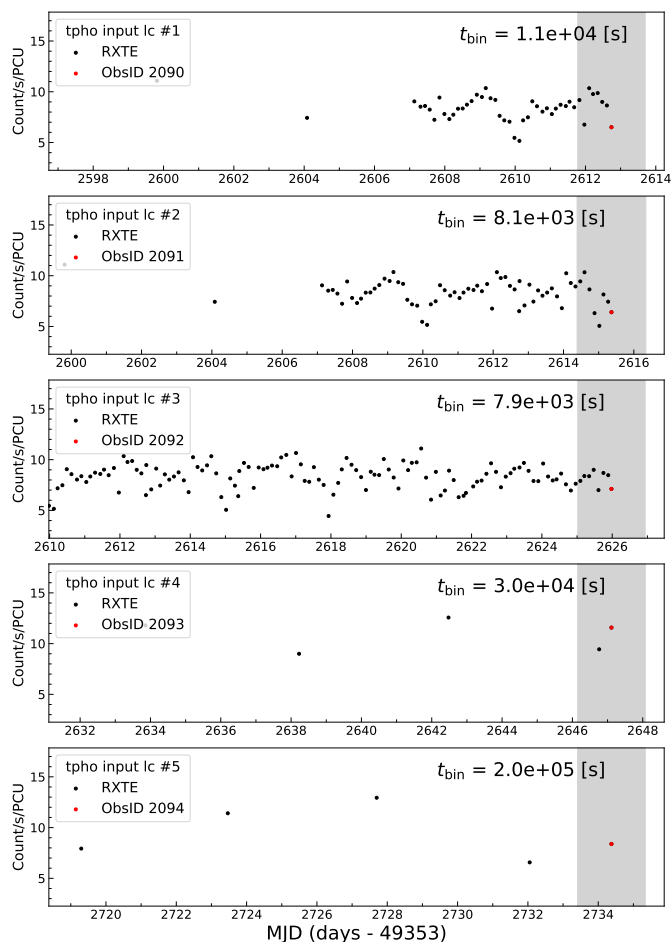


Fig. 4: RXTE light curve used as input for each `tpho` component calculation with the same starting data point from 1800 MJD. We show here the part of light curve within 14 days before the Chandra observation (red dot) corresponding to each component. The markers are similar to Fig. 3. t_{bin} (time resolution) in unit of second was defined by the time difference between the Chandra observation and the last RXTE observation before it.

pling uncertainties lead to too high uncertainties in the predicted transmission. We combine the results for the three comparisons of Fig. 8 in Fig. 9. The density corresponding to the minimum chi-square value of 128.76, which is $10^{13.4} \text{ m}^{-3}$, represents the best-fit solution confidently. At the 3σ confidence level, we find that the density is higher than $10^{12.3} \text{ m}^{-3}$. The conservative lower limit by the `tpho` model calculation indicates that the assumption of photoionization equilibrium (`pi on` in the horizontal solid line with $\chi^2 = 138$) is less accurate than the `tpho` predictions at the 3.1σ confidence level ($\chi^2 = 137$). Additionally, Our lower limit is at least two orders of magnitude higher compared to the estimate based on photoionization equilibrium by Krongold et al. (2005), who derived a density of $> 1 \times 10^{10} \text{ m}^{-3}$.

5. Discussion

Through our analysis of the extensive Chandra/HETGS data set from the 2001 NGC 3783 campaign, we have identified significant spectral variability within the 16–17 Å range, with the most notable changes occurring on a monthly timescale. This finding indicates that the flux variation is likely driven by long-term

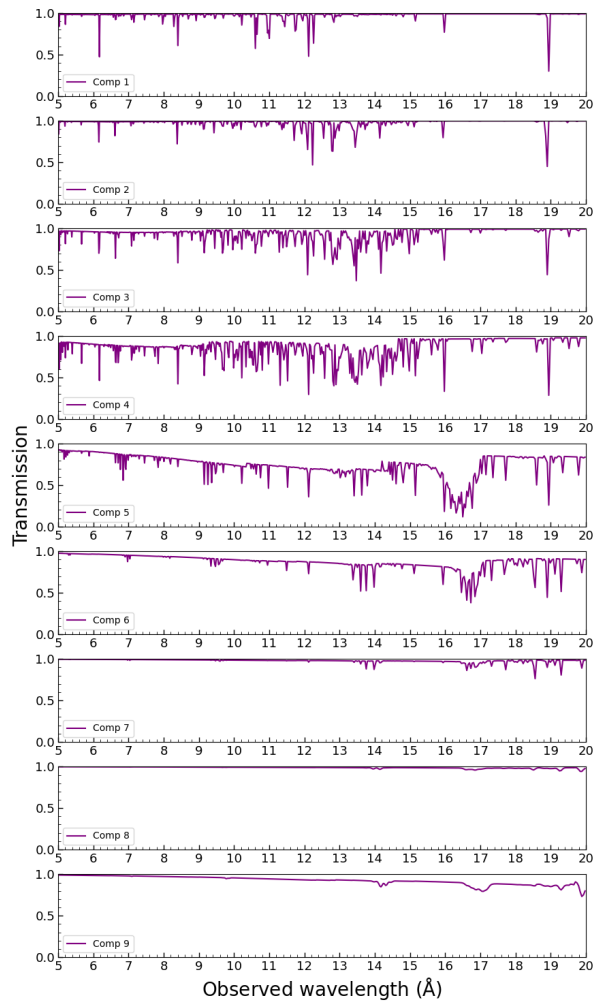


Fig. 5: Transmissions of the nine warm absorber components of NGC 3783 computed with the `pi on` model based on the parameters listed in Mao et al. (2019).

fluctuations (on the order of month or more), which influence the plasma state of the warm absorber. Time-dependent photoionization modeling using `tpho`, incorporating the RXTE light curve with a daily binning, suggests that the observed variability is predominantly attributable to component 5 of the warm absorber ($\log \xi = 1.65$). This component requires a density of at least $2.0 \times 10^{12} \text{ m}^{-3}$ to account for the variability, thus constraining its location to within 0.27 pc.

Our results confirm the flux-dependent features reported by Krongold et al. (2005). However, the density limits derived in our study are significantly higher than those presented in their work. This difference can likely be attributed to the advancements in our model, which employs the latest time-dependent photoionization calculations and updated atomic data. Additionally, our findings are consistent with the density range reported by Gu et al. (2023), who also utilized the `tpho` model but em-

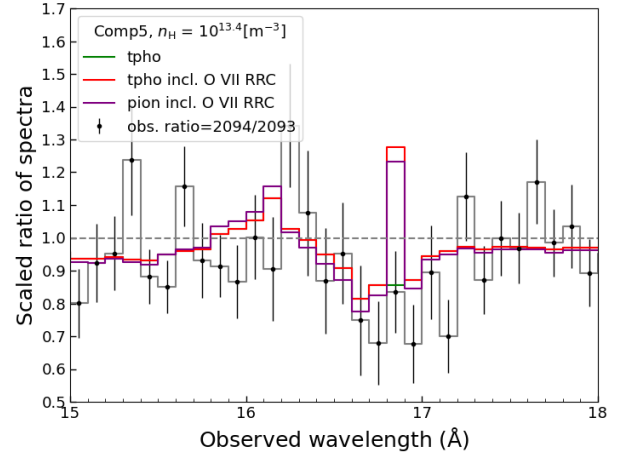
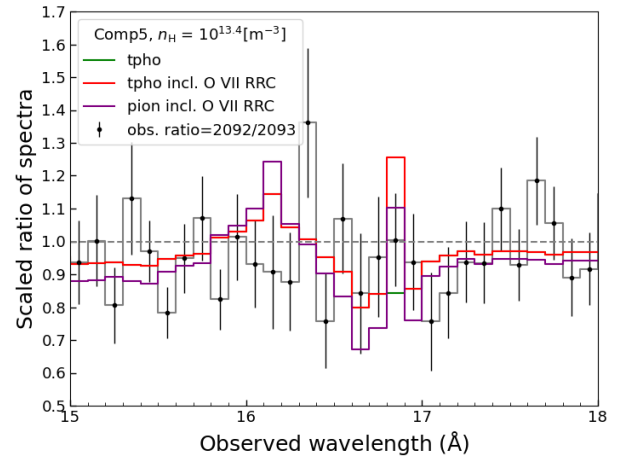
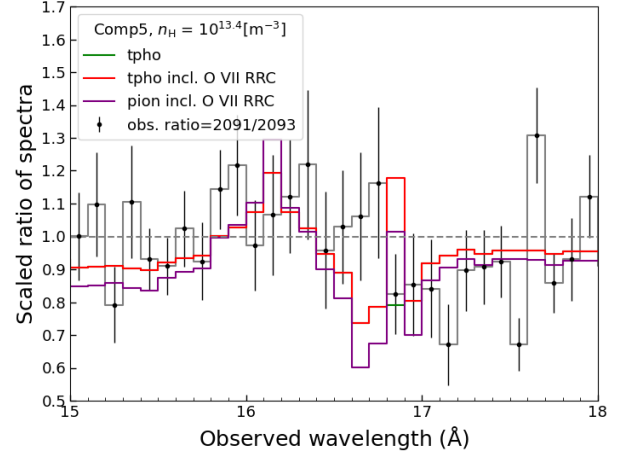
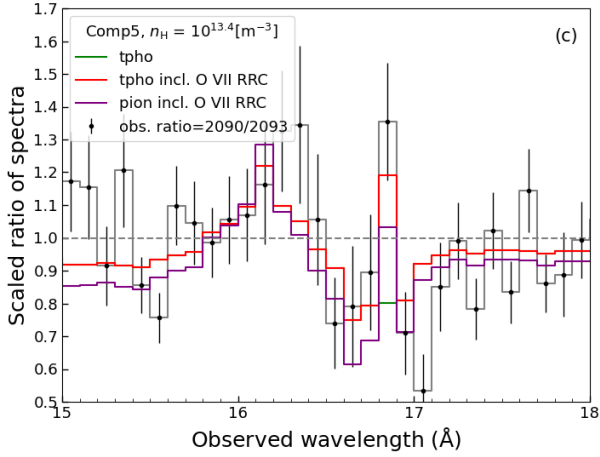
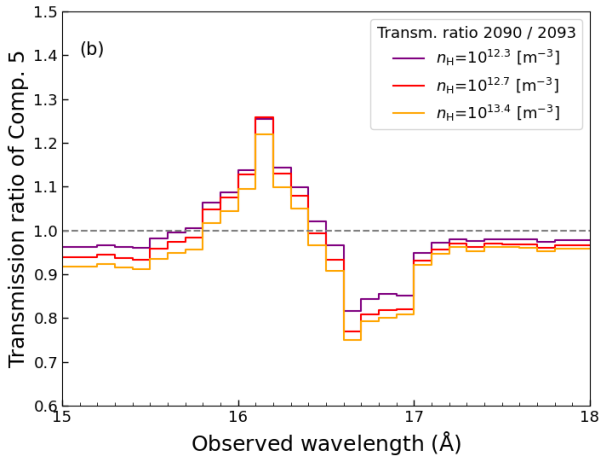
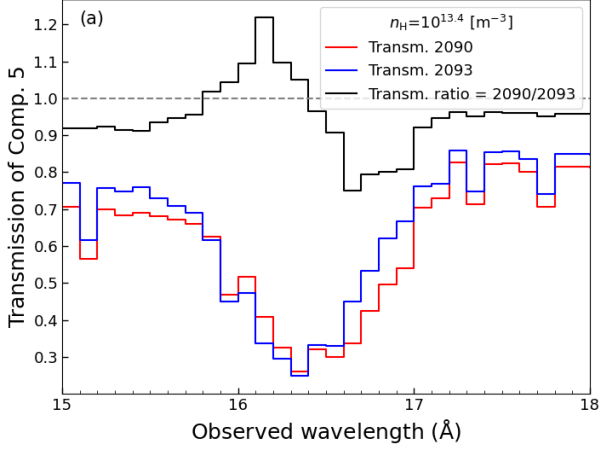


Fig. 6: tpho models for component 5 in the 15 – 18 Å binned with 0.1Å. (a) Transmission of component 5 in high flux state (blue) and low flux state (red), transmission ratio (black) from low flux state over high; (b) Transmission ratio of component 5 as a function of increasing density. (c) The observed ratio (black) was fitted well by the tpho model with a density of $10^{13.4} \text{ m}^{-3}$ including the O VII RRC feature (red). The local scaling factor of 2.21 was calculated from the counts in the 9 - 14 Å range.

Fig. 7: Best fitting of obs. ratio with model ratio for groups of ObsID 2091/2093, ObsID 2092/2093, ObsID 2094/2093, corresponding to the local scaling factor of 2.30, 1.87 and 1.66 respectively. The same approach was used as shown in Fig 6.

ployed a fundamentally different approach that focused solely on spectroscopic fitting of the time-averaged spectrum.

The soft excess reported by [Netzer et al. \(2003\)](#) and [Krongold et al. \(2005\)](#) could potentially introduce systematic uncertainties into our results, as the current tpho model does not ac-

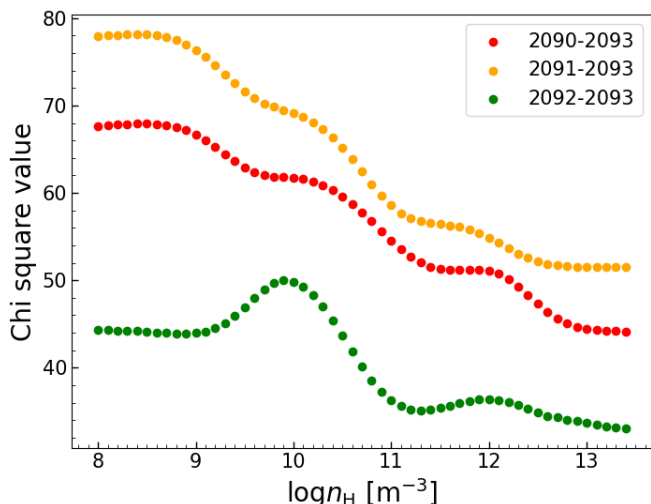


Fig. 8: Chi-square values computed from a comparison of observed spectral ratios with model ratios computed with the `tpho` model.

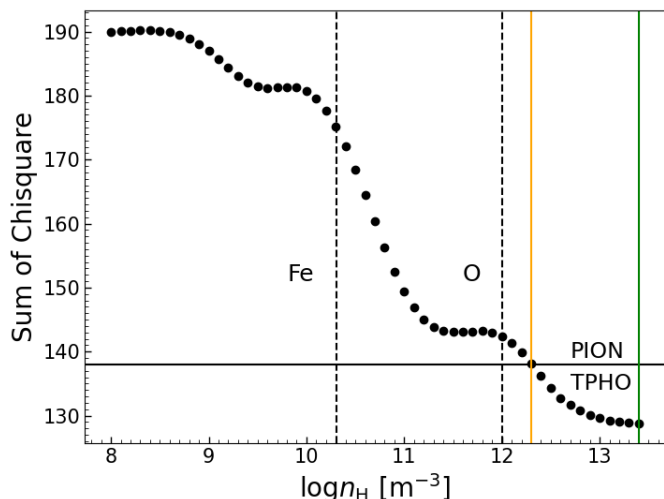


Fig. 9: Sum of chi-square values from Fig. 8 vs. density (black dots). The minimum chi-square value of 128.76 is obtained for a density of $10^{13.4} \text{ m}^{-3}$ (green line). The chi-square value for fits with the `pion` model is shown as a solid horizontal line, which is higher than the `tpho` value at the 3σ confidence level (orange line). The vertical dashed lines indicate the densities of the out-flow corresponding to a recombination time scale of 10^5 s for oxygen and iron.

count for changes in the SED. To assess the impact of the soft excess, we increased the flux in the $10 - 30 \text{ \AA}$ range by 20% and reran the `tpho` calculation for component 5. As shown in Figure 10, the soft excess has a negligible effect on the time variability of the Fe UTA and O edge within the relevant wavelength range, particularly in our fitting range.

Netzer et al. (2003) concluded that the observed changes in the underlying continuum were attributed to the appearance (high flux state) and disappearance (low flux state) of the soft excess component. This conclusion is consistent with the observations from ObsIDs 2093 and 2090, as shown in Fig. 1. The

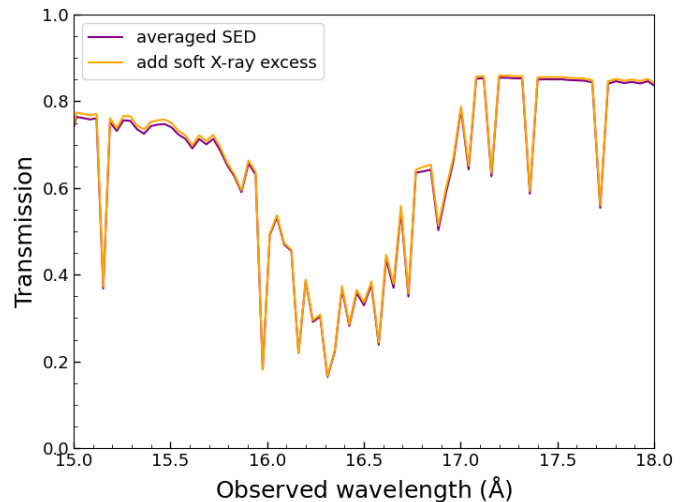


Fig. 10: Transmission of component 5 with `PION` calculation by using different SED. Purple: averaged SED, orange curve: adding soft X-ray excess in wavelength of $10 - 30 \text{ \AA}$.

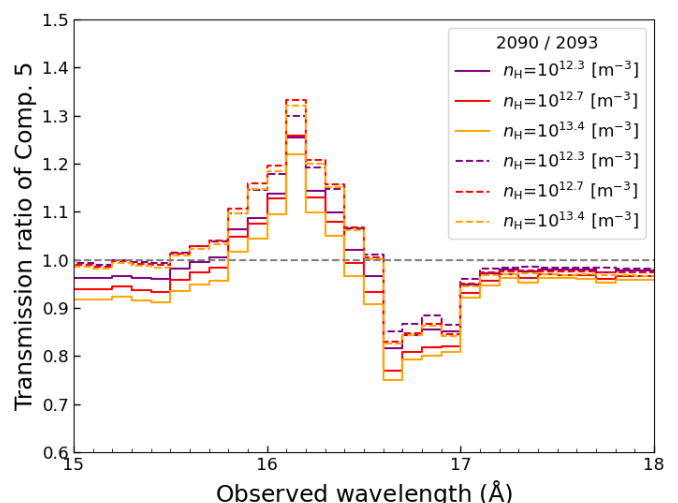


Fig. 11: Transmission ratio of component 5 with the `tpho` model for different density in solid and dashed lines (including or excluding oxygen, respectively).

significant Fe UTA structure observed in ObsID 2093, following ObsID 2090, suggests that the Fe charge state has changed on a monthly timescale according to `tpho` calculations, allowing us to constrain the density of the low-ionization component of the warm absorbers. Fig. 10 demonstrates that the soft X-ray excess does not significantly affect the Fe UTA feature, especially under the assumption of high density for the warm absorber component, as predicted by the `pion` model.

As illustrated in Figure 6, component 5 exhibits absorption features primarily from the Fe UTA and O VII edge at the relevant wavelengths. Due to their distinct recombination timescales—approximately 10^3 seconds for Fe and 10^5 seconds for O VII at a density of 10^{12} m^{-3} —Fe and O VII respond differently to source variations, with Fe reacting to more rapid fluctuations while O VII primarily reflects longer-term changes. To fully

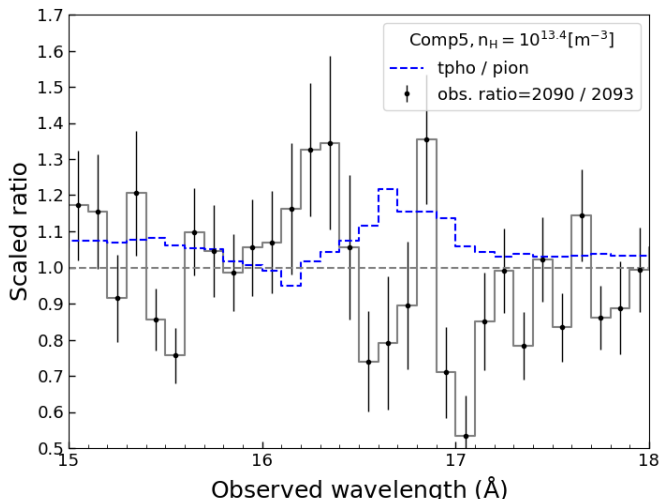


Fig. 12: Transmission ratio of tpho over pion is represented by the blue line, observation ratio of ObsID 2090 to 2093 was illustrated in black curve.

separate the spectral contributions from Fe and O VII, a detailed analysis of spectral variations on hour- and day-level timescales would be ideal, though such data are not immediately available in this study. However, an estimate of their relative contributions to the observed spectral ratio variation can still be obtained. By setting the oxygen column density to zero in the tpho calculation, we isolate the Fe UTA feature, represented as the dashed line, and compare it to the combined Fe and O VII calculation, shown as the solid line in Figure 11. The results suggest that Fe UTA absorption predominantly drives the variation in the 16–16.6 Å range, while the O VII edge contribution is secondary.

The comparison between the tpho and pion models, as shown in panel (c) of Figure 6 reveals subtle differences between the out-of-equilibrium and equilibrium assumptions, particularly in the 16.7–17 Å range, where the O VII edge contributes. By calculating the ratio of the tpho to the pion transmission ratios, shown as the blue line in Figure 12, we observe that in the Fe UTA band, the tpho model with a density of $10^{13.4} \text{ m}^{-3}$ matches closely with pion. However, in the 16.7–17 Å range, where the O VII edge impacts absorption, tpho shows a 10% difference from pion.

Considering this, and noting the slight decrease in continuum absorption in the pion model in Figure 6, we hypothesize that in ObsIDs 2090 and 2093, Fe has likely reached equilibrium while oxygen has not. This is due to the fact that the recombination timescale for Fe (100 seconds at $10^{13.6} \text{ m}^{-3}$) is considerably shorter than the light curve sampling interval, allowing Fe to reach equilibrium quickly (also refer to Figure 4). In contrast, oxygen, with a recombination timescale of approximately 10^4 s at the same density, aligns more closely with the sampling binsize, causing its response to lag behind the flux variations observed. Consequently, given the gaps between observations, oxygen could serve as an insightful diagnostic tool to probe higher-density plasmas, where recombination timescales more effectively reveal out-of-equilibrium effects (see Fig. 9). This further emphasizes the importance of considering both density and recombination timescales in characterizing plasma conditions in variable environments.

The upper limit of the density $n_{\text{H,upp}}$ for an escaping wind is derived from the assumption that the outflowing velocity v_{out} is larger than or equal to the escape velocity $v_{\text{esc}} = \sqrt{2GM_{\text{BH}}/r}$. This yields

$$n_{\text{H,upp}} = \frac{L_{\text{ion}} v_{\text{out}}^4}{4(GM_{\text{BH}})^2 \xi} \quad (2)$$

by substitute escaping velocity into Eq. 1. The lower limit density n_{H} of component 5 from our present tpho modelling is larger than $n_{\text{H,upp}}$ (see Figure 8 of Li et al. 2023), which indicates that the velocity of component 5 remains below the escape velocity. Therefore, this velocity discrepancy suggests that component 5 may be a failed wind, unable to reach velocities sufficient to escape the gravitational pull of the SMBH, thus remaining bound to the system.

Based on the density constraints shown in Figure 9, we can constrain the distance r of the low-ionization warm absorber component using Eq. 1. Inserting $\log \xi = 1.65$, $L_{\text{ion}} = 6.36 \times 10^{36} \text{ W}$ (Mehdipour et al. 2017), at the 3σ confidence level, the distance of component 5 is limited to less than 0.27 pc. The derived distance is notably closer to the central SMBH than previous estimates, such as the $\leq 6 \text{ pc}$ derived by Krongold et al. (2005). This closer proximity aligns well with density values inferred from other variability studies, such as the upper bounds suggested by Behar et al. (2003) based on XMM-Newton grating spectra analysis. Furthermore, this finding of location is consistent with the modelling by Chelouche & Netzer (2005), who predicted that hot X-ray absorbers likely originate from within 1 pc by analyzing thermodynamic conditions in the outflowing structures.

Combining the results from the GRAVITY Collaboration et al. (2021), the upper distance limit for component 5 (0.27 pc) is smaller than the coronal line region (CLR, 0.4 pc) but larger than the hot dust (0.14 pc) and broad line region (BLR, 16 light-days) as measured by Br γ . This is consistent with the predicted scenario of a low-ionization radiatively-driven wind, which fails to escape and returns to the disk (Gallo et al. 2023).

This "failed wind" component could provide a physical framework for interpreting various phenomenological components of AGN (Giustini & Proga 2021). For instance, the inner failed wind component might offer a physical interpretation for key AGN features, such as the high-ionization BLR, the obscuring material, and the X-ray corona. Additionally, the failed wind solutions describing the inner accretion and ejection flows of AGN could help assess whether they significantly alter the physical and geometrical structure of the innermost accretion flow around highly accreting SMBHs.

In any model that predicts the launching mechanism and the impact of outflows on the surrounding medium, it is essential to determine the precise distance at which the outflow is launched. Time-dependent photoionization modelling, which incorporates the variability of the warm absorber, offers an advantage in accurately determining the gas density. High-sensitivity, high-resolution calorimeters (such as Resolve onboard XRISM, Tashiro et al. 2020, and X-IFU prepared for the future Athena X-ray observatory, Barret et al. 2018) will provide significant advancements, especially in the study of variable warm absorbers and in determining their gas densities.

6. Conclusions

In this study, we revisited the unobscured-state spectrum of NGC 3783 using archival Chandra/HETGS data from the 2001 cam-

paigned, investigating spectral variability over timescales of several months by comparing ratio spectra across varying flux levels. Significant changes were observed in the ratio spectrum over week-to-month timescales, corresponding to a flux variation factor of $1.4 - 2$. This variability, detected at a significance level greater than 10σ at maximum flux, points to a notable response in the ionizing continuum. To further explore these changes, we applied time-dependent photoionization modelling with `tpho` (SPEX) and found that the low-ionization component ($\log\xi = 1.65$) exhibits a pronounced sensitivity to flux variations in the Fe UTA band. We constrained the density of this low-ionization component to be higher than $10^{12.3} \text{ m}^{-3}$ at the 3σ confidence level. This density places the location of the component within 0.27 pc of the central source. Our results suggest that this low-ionization component may represent a failed wind candidate, as it lacks sufficient momentum to escape the gravitational influence of the SMBH, instead remaining bound within the system. This finding contributes to a refined understanding of the dynamics and structure of AGN outflows in NGC 3783.

Acknowledgements. We thank the anonymous referee for his/her constructive comments. C.L. acknowledges support from Chinese Scholarship Council (CSC) and Leiden University/Leiden Observatory, as well as SRON. SRON is supported financially by NWO, the Netherlands Organization for Scientific Research. C.L. thanks Elisa Costantini for the discussions of distance scale of outflowing wind.

References

- Alloin, D., Santos-Lleo, M., Peterson, B. M., et al. 1995, *A&A*, 293, 293
 Ballhausen, R., Kallman, T. R., Gu, L., & Paerels, F. 2023, *ApJ*, 956, 65
 Barret, D., Lam Trong, T., den Herder, J.-W., et al. 2018, in *Society of Photo-Optical Instrumentation Engineers (SPIE) Conference Series*, Vol. 10699, *Space Telescopes and Instrumentation 2018: Ultraviolet to Gamma Ray*, ed. J.-W. A. den Herder, S. Nikzad, & K. Nakazawa, 106991G
 Behar, E., Rasmussen, A. P., Blustin, A. J., et al. 2003, *ApJ*, 598, 232
 Behar, E., Sako, M., & Kahn, S. M. 2001, *ApJ*, 563, 497
 Bentz, M. C., Williams, P. R., Street, R., et al. 2021, *ApJ*, 920, 112
 Blustin, A. J., Branduardi-Raymont, G., Behar, E., et al. 2002, *A&A*, 392, 453
 Chelouche, D. & Netzer, H. 2005, *ApJ*, 625, 95
 Davies, R., Baron, D., Shimizu, T., et al. 2020, *MNRAS*, 498, 4150
 Davies, R. I., Burtscher, L., Rosario, D., et al. 2015, *ApJ*, 806, 127
 Gabel, J. R., Kraemer, S. B., Crenshaw, D. M., et al. 2005, *ApJ*, 631, 741
 Gallo, L. C., Miller, J. M., & Costantini, E. 2023, *arXiv e-prints*, arXiv:2302.10930
 Giustini, M. & Proga, D. 2021, in *IAU Symposium*, Vol. 356, *Nuclear Activity in Galaxies Across Cosmic Time*, ed. M. Pović, P. Marziani, J. Masegosa, H. Netzer, S. H. Negu, & S. B. Tessema, 82–86
 GRAVITY Collaboration, Amorim, A., Bauböck, M., et al. 2021, *A&A*, 648, A117
 Gu, L., Kaastra, J., Rogantini, D., et al. 2023, *A&A*, 679, A43
 Juráňová, A., Costantini, E., & Uttley, P. 2022, *MNRAS*, 510, 4225
 Kaastra, J. S., Detmers, R. G., Mehdipour, M., et al. 2012, *A&A*, 539, A117
 Kaastra, J. S., Mehdipour, M., Behar, E., et al. 2018, *A&A*, 619, A112
 Kaastra, J. S., Mewe, R., & Nieuwenhuijzen, H. 1996, in *UV and X-ray Spectroscopy of Astrophysical and Laboratory Plasmas*, ed. K. Yamashita & T. Watanabe, 411–414
 Kaastra, J. S., Raassen, A. J. J., de Plaa, J., & Gu, L. 2024, *SPEX X-ray spectral fitting package*, (3.08.01). Zenodo.
 Kaspi, S., Brandt, W. N., George, I. M., et al. 2002, *ApJ*, 574, 643
 Krolik, J. H., McKee, C. F., & Tarter, C. B. 1981, *ApJ*, 249, 422
 Krongold, Y., Nicastro, F., Brickhouse, N. S., et al. 2003, *ApJ*, 597, 832
 Krongold, Y., Nicastro, F., Brickhouse, N. S., Elvis, M., & Mathur, S. 2005, *ApJ*, 622, 842
 Li, C., Kaastra, J. S., Gu, L., & Mehdipour, M. 2023, *A&A*, 680, A44
 Mao, J., Kaastra, J. S., Mehdipour, M., et al. 2017, *A&A*, 607, A100
 Mao, J., Mehdipour, M., Kaastra, J. S., et al. 2019, *A&A*, 621, A99
 Mehdipour, M., Kaastra, J. S., Kriss, G. A., et al. 2017, *A&A*, 607, A28
 Netzer, H., Kaspi, S., Behar, E., et al. 2003, *ApJ*, 599, 933
 Rogantini, D., Mehdipour, M., Kaastra, J., et al. 2022, *ApJ*, 940, 122
 Sadaula, D. R., Bautista, M. A., García, J. A., & Kallman, T. R. 2023, *ApJ*, 946, 93
 Silva, C. V., Uttley, P., & Costantini, E. 2016, *A&A*, 596, A79
 Tarter, C. B., Tucker, W. H., & Salpeter, E. E. 1969, *ApJ*, 156, 943
 Tashiro, M., Maejima, H., Toda, K., et al. 2020, in *Society of Photo-Optical Instrumentation Engineers (SPIE) Conference Series*, Vol. 11444, *Space Telescopes and Instrumentation 2020: Ultraviolet to Gamma Ray*, ed. J.-W. A. den Herder, S. Nikzad, & K. Nakazawa, 1144422
 Theureau, G., Bottinelli, L., Coudreau-Durand, N., et al. 1998, *A&AS*, 130, 333